

Influence of the Formation Current Density on the Transport Properties of Galvanostatically Formed Model-Type Solid Electrolyte Interphases

Sebastian Kranz⁺^[a], Tobias Kranz⁺^[a], Tim Graubner,^[a] Yuriy Yusim,^[a] Lukas Hellweg,^[a] and Bernhard Roling^{*[a]}

During the production of commercial lithium-ion batteries, the solid electrolyte interphase (SEI) on the graphite particles of the negative electrode is typically formed through galvanostatic protocols with low current densities. Consequently, SEI formation is a time-consuming and rather expensive production step. In order to better understand the influence of the formation current density on the transport of ions and molecules across the SEI, we formed model-type SEIs on planar glassy carbon electrodes under galvanostatic control. In accordance with the

expectations from electrochemical nucleation and growth theory, we find that the transport of both ions and molecule becomes slower with increasing formation current density. However, it is remarkable that the ion transport is slowed down more strongly than the molecule transport. We show that at high formation current densities of about $-71 \mu\text{A cm}^{-2}$, our model-type SEIs clearly exceed the area-specific resistance tolerable in commercial lithium-ion cells.

1. Introduction

The solid electrolyte interphase (SEI) is a crucial component of state-of-the-art lithium-ion batteries. It is a passivation layer, which is formed during the first charging of a lithium-ion battery on the surface of the graphite anode and which impedes further decomposition of the carbonate-based electrolyte. In the ideal case, the SEI is highly permeable for Li^+ ions, but suppresses molecule and electron transport completely.^[1] However, real SEIs allow for a slow ongoing decomposition of the electrolyte, which leads to a slow growth of the SEI and to an increasing SEI resistance during cycling of the battery.^[2,3] This SEI ageing is an important degradation mechanism of lithium-ion batteries, which reduces their cycle life. Usually, SEI-forming salts or molecules are added to the electrolyte in order to improve the mechanical, morphological and electrochemical properties of the SEI and to slow down SEI ageing.^[4–6] One of these additives is lithium bis(oxalate)borate (LiBOB), which is known to form stable SEIs, but also to increase the ion transport resistance of the SEI.^[6–8]

At present, the interrelation between the SEI formation conditions and the transport properties of the SEI are not well understood.^[9] During the production of commercial battery

cells, the SEI formation is usually carried out under galvanostatic control.^[10,11] Low current densities are typically applied to ensure a stable and properly passivating SEI.^[12–14] Consequently, SEI formation is a time-consuming process, which contributes significantly to the production costs of a battery.^[10] The application of higher formation currents without deteriorating the SEI properties would therefore be highly desirable.

Consequently, the question arises why high formation current densities are problematic for the SEI properties. During SEI formation, reduction processes lead to the nucleation and growth of solid phases on top of the graphite particles. In electrochemical nucleation and growth theory, a high current density and a high overpotential lead to a small size of the critical nuclei and to a high nucleation rate.^[15] A large number of small crystal nuclei on the electrode surface results typically in the formation of thin and dense layers. A well-known example is the formation of Li_2O_2 layers on the cathode during discharging of $\text{Li}-\text{O}_2$ batteries. A higher cathodic overpotential and current density favors the formation of thin and dense Li_2O_2 layers.^[16] Consequently, one might expect that higher formation current densities lead also to the formation of denser and better passivating SEIs, which should be advantageous for the battery cycle life. However, contradictory experimental results have been published in the literature. Bhattacharya et al. reported that voltammetric SEI formation with low scan rates and accordingly low current densities leads to a higher coverage of the graphite particles with a more uniform SEI than SEI formation with high scan rates and high current densities.^[12,13] Antonopoulos et al. concluded that a high overpotential during SEI formation leads to a more open and granular SEI structure on the graphite particles, whereas formation with a low overpotential yields a smooth and less permeable SEI.^[11,17] Märkle et al., on the other hand, reported that a higher

[a] S. Kranz,⁺ T. Kranz,⁺ T. Graubner, Y. Yusim, L. Hellweg, Prof. B. Roling
Department of Chemistry and Center for Materials Science (WZMW)
University of Marburg
Hans-Meerwein-Straße 4, 35032 Marburg, Germany
E-mail: roling@staff.uni-marburg.de

⁺[+] These authors contributed equally to this work

 Supporting information for this article is available on the WWW under
<https://doi.org/10.1002/batt.201900110>

 © 2019 The Authors. Published by Wiley-VCH Verlag GmbH & Co. KGaA. This is an open access article under the terms of the Creative Commons Attribution License, which permits use, distribution and reproduction in any medium, provided the original work is properly cited.

overpotential during SEI formation yields a smoother SEI, which suppresses exfoliation of graphite during Li intercalation.^[18]

Due to these contradictory experimental results on graphite SEIs and due to the high interest in faster SEI formation in commercial battery production, we carried out a systematic study on galvanostatic formation of model-SEIs on planar glassy carbon electrodes. In previous studies, it was shown that such model-type planar electrodes are well suited for studying the transport of ions and molecules across the SEI.^[19–26] This is in contrast to graphite composite electrodes, which exhibit a very complex morphology strongly complicating the understanding of transport processes. In order to favor the formation of SEIs with good passivating properties, we used LiBOB as electrolyte additive and we carried out galvanostatic SEI formation at different current densities. The transport of ions and molecules across the SEI was characterized by means of electrochemical impedance spectroscopy and redox-probe voltammetry. In addition, thicknesses and morphological properties of the galvanostatically formed SEIs were studied by scratching experiments with an atomic force microscope tip. We show that high formation current densities lead to strongly differing effective diffusion coefficients of ions and molecules in the SEI, in contrast to the previously reported results on SEIs formed by slow-scan voltammetry.

Experimental Section

Cell Assembly

The electrochemical experiments were conducted inside an airtight TSC SURFACE-Cell (RHD INSTRUMENTS GMBH & Co. KG). Lithium foil (Rockwood LITHIUM) was used as counter and reference electrode. Consequently, in the following, all potentials are given vs. Li/Li⁺. SIGRADUR-G glassy carbon (HTW HOCHTEMPERATUR-WERKSTOFFE GMBH) was used as working electrode. The electrode area in the cell was determined by an O-ring (EPDM) with a diameter of 0.6 cm (active area: 0.28 cm²). The glassy carbon (GC) plates were freshly polished prior to the electrochemical measurements by using sequentially KEMET[®] diamond suspension with an average particle diameter of 3 µm, 1 µm and 0.25 µm, respectively, and then cleaned with HPLC grade acetone. After polishing and cleaning, the root mean square roughness of the GC plates was of about 1–2 nm. The electrolytes were prepared by mixing 1 M LiPF₆ in 50/50 (vol/vol) ethylene carbonate/ethyl methyl carbonate (EC/EMC) with 1 M LiPF₆ solved in dimethyl carbonate (DMC) (all solutions were purchased from SIGMA ALDRICH; H₂O < 20 ppm). The final electrolyte composition was 1 M LiPF₆ in 3/3/4 EC/EMC/DMC. For the LiBOB-containing electrolyte, the LiBOB salt (SIGMA ALDRICH) was dissolved in the electrolyte solution to obtain a molar additive concentration of 50 mM. This is a typical concentration for LiBOB as electrolyte additive.^[6,27] The airtight cells were assembled inside a glovebox under argon atmosphere (H₂O and O₂ < 1 ppm). The cells were then removed from the glovebox, and the measurements were performed outside the glovebox at room temperature (25 °C), if not otherwise stated.

SEI Formation and Electrochemical Measurements

For SEI formation and all subsequent electrochemical measurements, a Multi Autolab/M101 equipped with a FRA32 M impedance

module from METROHM AUTOLAB BV was used. For the galvanostatic SEI formation, cathodic current densities of $-4 \mu\text{Acm}^{-2}$, $-18 \mu\text{Acm}^{-2}$, and $-71 \mu\text{Acm}^{-2}$, respectively, were applied, until the cutoff limit of 0.01 V vs Li/Li⁺ was reached. Afterwards the cell was rested for two hours at OCP conditions (approximately 3 V). Then a second galvanostatic discharge was performed in order to confirm the passivation of the electrode. SEI formation via slow-scan cyclic voltammetry was conducted with a scan rate of 0.5 mV s⁻¹ in the voltage range between 3 V to 0.01 V for three cycles.

Before and after SEI formation, impedance spectroscopy was applied. To this end, the cell was stabilized at 3 V vs Li/Li⁺ for 20 min. The impedance measurements were done in a frequency range from 10⁵ Hz to 0.03 Hz with a root mean square AC voltage of 5 mV. Impedance spectra was analyzed using the software RelaxIS 3. The Circuit Simulator 3 implemented in this software was used for simulating impedance and elastance spectra. Subsequently, the electrolyte was replaced inside the glovebox by an electrolyte with the same composition, but containing in addition a concentration of 10 mM ferrocene (98%, Acros Organics). Then impedance spectra were taken at 3 V, followed by a voltammogram between 3 V and 3.45 V (half wave potential of ferrocene = 3.24 V) with a scan rate of 10 mV/s.

Temperature-dependent EIS and voltammograms were performed by using a Microcell HC – Basic Package for closed cells cell stand (RHD INSTRUMENTS GMBH & Co. KG) and thermo controlling unit (Eurotherm 3216).

AFM

A CYPHER AFM (ASYLUM RESEARCH) equipped with a boron-doped diamond tip FM-LC (ADAMA INNOVATIONS) was used to conduct scratching experiments on the SEIs. After an SEI had been formed galvanostatically, the glassy carbon electrode was removed from the cell inside a glovebox, was rinsed with DMC and was dried under inert atmosphere. Then, the electrode was mounted into the environmental scanner of the CYPHER AFM. The airtight environmental scanner with the sample under inert atmosphere was then removed from the glovebox and mounted into the CYPHER AFM. First, the surface of the SEI was scanned in tapping mode to prevent mechanical damages to the SEI surface. Afterwards, the SEI was scratched with a force of up to 1.5 µN in order to successively remove parts of the SEI until reaching the GC surface. The AFM data were analyzed using the software GWYDDION 2.51.

2. Results and Discussion

2.1. Influence of Formation Current Density on Transport across the SEI

In Figure 1, we plot the glassy carbon electrode potential during galvanostatic SEI formation in the LiBOB-containing electrolyte versus the charge flow. Three different formation current densities $-4 \mu\text{Acm}^{-2}$, $-18 \mu\text{Acm}^{-2}$, and $-71 \mu\text{Acm}^{-2}$, respectively, were applied. When starting the experiment, the electrode potential jumps from the OCP to about 1.75 V, where the reductive decomposition of LiBOB takes place. After a certain amount of charge flow, the potential jumps to about 0.5 V, implying the reductive decomposition of the carbonate molecules. While the charge flow due to LiBOB decomposition decreases with increasing formation current, the charge flow

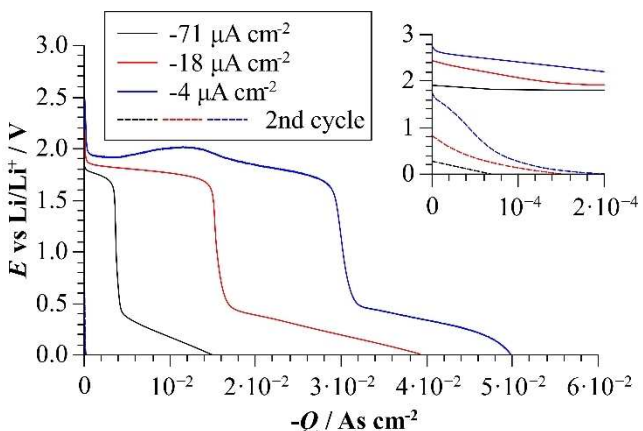


Figure 1. Electrode potential vs. charge profiles for galvanostatic SEI formation of a LiBOB-containing electrolyte on a glassy carbon electrode at current densities of $-71 \mu\text{A cm}^{-2}$, $-18 \mu\text{A cm}^{-2}$ and $-4 \mu\text{A cm}^{-2}$, respectively. The inset shows potential vs. charge profiles for the second SEI formation cycle.

during carbonate decomposition depends only weakly on the formation current. Thus, the overall charge flow and the overall amount of electrolyte decomposition decreases with increasing formation current. The potential vs. charge profile implies that the LiBOB decomposition is not sufficient to passivate the electrode, but an additional carbonate decomposition is necessary. After the first complete SEI formation cycle, the charge flow in the second cycle is about 2 orders of magnitude

lower, see inset of Figure 1, proving a clear passivation of the electrode.

In Figure 2 (a)–(c), we show impedance spectra of the GC | electrolyte interface after galvanostatic SEI formation. The spectra were taken at a potential of 3 V vs Li/Li⁺, at which no Faradaic processes take place. At a formation current density of $-4 \mu\text{A cm}^{-2}$, the high-frequency part of the spectrum is determined by the SEI impedance, followed by electrode polarization at low frequencies. The SEI semicircle is not completely visible, however, there is a clear turning point in the spectra, at which the SEI semicircle crosses over into the electrode polarization. We fitted the $\tilde{Z}(\omega)$ spectrum with the equivalent circuit shown in the inset. This equivalent circuit is composed of a resistor R_{el} describing the bulk electrolyte resistance, a parallel $R_{SEI} || CPE_{SEI}$ element representing the resistance and the capacitance of the SEI, and a parallel $R_{CT} || CPE_{DL}$ representing the charge transfer resistance and the double layer capacitance, respectively. The impedance of a constant-phase element (CPE) is given by $Z_{CPE} = Q^{-1}(i\omega)^{-\alpha}$ with $\alpha \leq 1$. From the fit, we obtain an SEI resistance of $R_{SEI} = 1 \text{ k}\Omega \text{cm}^2$. For the SEIs formed at $-18 \mu\text{A cm}^{-2}$ and $-71 \mu\text{A cm}^{-2}$, the uncertainty of the R_{SEI} values is large, since the SEI semicircle strongly overlaps with the $R_{CT} || CPE_{DL}$ impedance contribution. Consequently, we can only deduce approximate values for the SEI resistance from the fits in the $\tilde{Z}(\omega)$ plane. These are about $50 \text{ k}\Omega \text{cm}^2$ and about $200 \text{ k}\Omega \text{cm}^2$ for the SEIs formed at $-18 \mu\text{A cm}^{-2}$ and at $-71 \mu\text{A cm}^{-2}$, respectively.

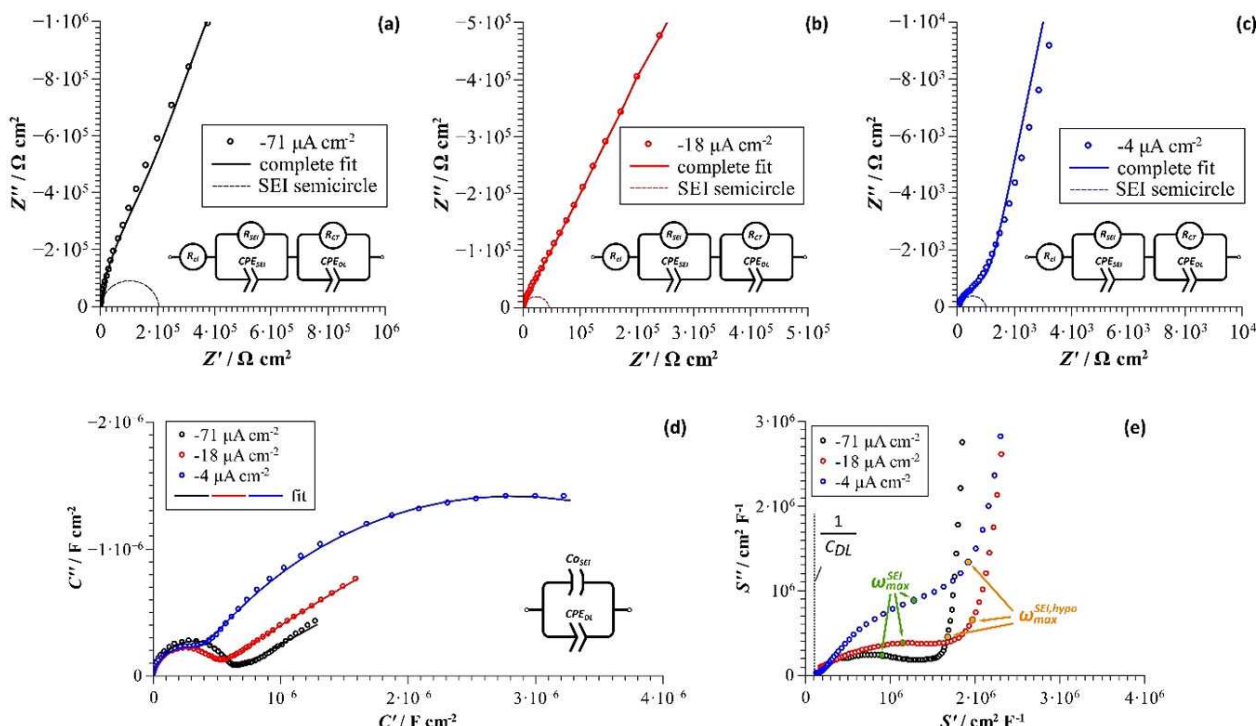


Figure 2. Impedance, capacitance and elastance spectra of the glassy carbon electrode after galvanostatic SEI formation at different current densities. a)–c) Nyquist impedance plots for current densities of $-71 \mu\text{A cm}^{-2}$, $-18 \mu\text{A cm}^{-2}$ and $-4 \mu\text{A cm}^{-2}$, respectively. d) Complex capacitance plots for all three current densities. e) Complex elastance plots for all three current densities.

In order to obtain more precise values for the resistance and capacitance of the SEIs formed at $-18 \mu\text{A cm}^{-2}$ and $-71 \mu\text{A cm}^{-2}$, it turned out to be helpful to consider in addition the complex capacitance spectra $\hat{C}(\omega)$ and the complex elastance spectra $\hat{S}(\omega)$ [Eqs. (1) and (2)]:

$$\hat{C}(\omega) = \frac{1}{i\omega \hat{Z}(\omega)} = C' + iC'' \quad (1)$$

$$\hat{S}(\omega) = i\omega \hat{Z}(\omega) = S' + iS'' \quad (2)$$

where i =imaginary unit and ω =angular frequency.

In principle, all spectra contain the same information. However, it is well known that specific features in impedance data can be more easily visible in specific data presentations than in others.^[28] In Figure 2 (d), we show a complex capacitance plot after SEI formation at different current densities. A clear high-frequency semicircle due to the existence of the SEI is visible. The semicircle can be fitted by a Cole-Cole expression [Eq. (3)]:

$$\hat{C}_j(\omega) = \frac{\Delta C}{1 + (i\omega\tau_j)^a} \quad (3)$$

with ΔC given by Equation (4):

$$\Delta C = \left(\frac{1}{C_{SEI}} + \frac{1}{C_{DL}} \right)^{-1} \approx C_{SEI} \quad (4)$$

The second approximation in equation (4) is based on the fact that C_{SEI} is around $0.4\text{--}0.8 \mu\text{F cm}^{-2}$, while C_{DL} is in the range of $10 \mu\text{F cm}^{-2}$. The values obtained for C_{SEI} from the Cole-Cole fit are close to the values obtained from the fit of the impedance

data. From these capacitance values, the thickness of the SEI can be estimated using Equation (5):

$$d_{SEI} = \frac{\varepsilon_0 \varepsilon_r A}{C_{SEI}} \quad (5)$$

where ε_0 =vacuum permittivity, ε_r =relative permittivity of the SEI, and A =electrode area.

In previous studies, we have shown that assuming relative permittivity values for the SEI in the range of $\varepsilon_r=10\text{--}20$ yields good agreement between the thickness estimated from impedance spectroscopy, d_{EIS} , and the thickness of the passivating inner layer of the SEI from AFM-based scratching experiments and FIB/SEM imaging.^[19,20] Assuming $\varepsilon_r=10$, we obtain d_{EIS} values of 22 nm, 19 nm and 14 nm for current densities of $-4 \mu\text{A cm}^{-2}$, $18 \mu\text{A cm}^{-2}$, and $-71 \mu\text{A cm}^{-2}$, respectively. This indicates that thinner SEI layers are formed with increasing current density, in accordance with the results for the charge flow during SEI formation shown in Figure 1.

Since elastance $\hat{S}(\omega)$ plots are not common in electrochemistry, we sketch simulated impedance and elastance spectra for an idealized equivalent circuit in Figure 3, in which the CPE elements CPE_{SEI} and CPE_{DL} used in Figure 2 are replaced by ideal capacitances C_{SEI} and C_{DL} . The following parameters were used for the simulation: $R_{el}=250 \Omega \text{cm}^2$, $R_{SEI}=10^4 \Omega \text{cm}^2$, $R_{CT}=10^6 \Omega \text{cm}^2$, $C_{SEI}=10^{-6} \text{F cm}^{-2}$, $C_{DL}=10^{-5} \text{F cm}^{-2}$. Note that in the simulated $\hat{S}(\omega)$ spectrum in Figure 3 (b), the frequency increases from the origin to high S' and S'' values. The vertical spike at high frequencies reflects the electrolyte resistance, while the intermediate frequency semicircle reflects the SEI properties. The SEI semicircle extends from $S' = \frac{1}{\Delta C} \approx \frac{1}{C_{SEI}}$ at high frequencies to $S' = \frac{1}{C_{DL}}$ at low frequencies, with the angular frequency of the S' maximum being given by Equation (6):

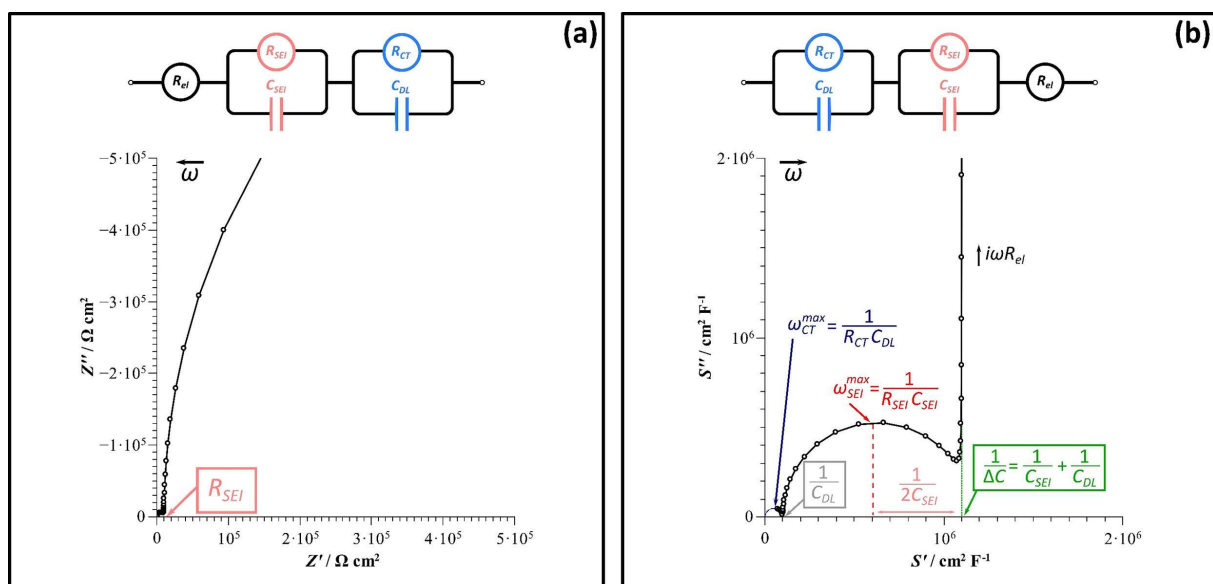


Figure 3. a) Simulated impedance and b) simulated elastance spectrum of the equivalent circuit with the following parameters: $R_{el}=250 \Omega \text{cm}^2$, $R_{SEI}=10^4 \Omega \text{cm}^2$, $R_{CT}=10^6 \Omega \text{cm}^2$, $C_{SEI}=10^{-6} \text{F cm}^{-2}$, $C_{DL}=10^{-5} \text{F cm}^{-2}$. The physical meaning of the circuit elements is given in the text.

$$\omega_{max}^{SEI} = \frac{1}{R_{SEI} C_{SEI}} \quad (6)$$

Here it is important to note that while in the $\hat{Z}(\omega)$ spectra in Figure 3 (a), the SEI semicircle is very small as compared to the $R_{CT} || C_{DL}$ semicircle, and the semicircles are not well separated, the opposite is true after conversion of the data into the $\hat{S}(\omega)$ plane in Figure 3 (b). This shows that an elastance plot is very well suited for analyzing the SEI properties. This holds true even in the case of SEI impedances, which are described by a parallel $R || CPE$ element, see Supporting Information.

In Figure 2 (e), the experimental data are shown in the $\hat{S}(\omega)$ -plane. Both the high-frequency spike caused by the electrolyte resistance and the intermediate-frequency semicircle reflecting the SEI properties are clearly visible. Extrapolating the high-frequency spike to the S' -axis results in $\Delta C \approx C_{SEI}$ values in good agreement with those obtained from the complex capacitance plane. At low frequencies, S' approaches values of about $10^5 \text{ cm}^2 \text{ F}^{-1}$, which is close to an inverse double layer capacitance of $10 \mu\text{F cm}^{-2}$. The low-frequency semicircle due to double layer formation and charge transfer, shown in the simulated spectra in Figure 3, is not visible in the experimental spectra, since due to the large charge transfer resistance, the angular frequency $\omega_{CT} = \frac{1}{R_{CT} C_{DL}}$ is outside the frequency window of the measurements. However, since the intermediate-frequency semicircle is clearly detectable, we can use the angular frequency of the S' maximum, $\omega_{max}^{SEI} = \frac{1}{R_{SEI} C_{SEI}}$, to calculate the SEI resistance R_{SEI} . R_{SEI} values of $0.8 \text{ k}\Omega \text{ cm}^2$, $17 \text{ k}\Omega \text{ cm}^2$, and $420 \text{ k}\Omega \text{ cm}^2$ were obtained for current densities of $-4 \mu\text{A cm}^{-2}$, $-18 \mu\text{A cm}^{-2}$, and $-71 \mu\text{A cm}^{-2}$, respectively. These values are listed in Table 1 and show clearly that the SEI resistance increases strongly with increasing formation current density.

Using the Nernst-Einstein equation, the effective diffusion coefficient of the Li^+ ions can be estimated by means of Equation (7), assuming identical diffusivities of cations and anions:^[19,20]

$$D_{Li^+}^{eff} = \frac{H_R RT}{2F^2 \cdot C_{LiPF_6}} \sigma_{SEI} = \frac{H_R RT}{2F^2} \frac{\varepsilon_0 \varepsilon_r}{R_{SEI} C_{SEI}} = \frac{H_R RT}{2F^2} \varepsilon_0 \varepsilon_r \omega_{max}^{SEI} \quad (7)$$

where H_R = Haven ratio = $1.72 = 1/0.58$,^[29] R = ideal gas constant; T = temperature; C_{LiPF_6} = concentration of lithium salt.

From this equation, we obtain $D_{Li^+}^{eff}$ values of $6.4 \cdot 10^{-13} \text{ cm}^2 \text{ s}^{-1}$, $2.5 \cdot 10^{-14} \text{ cm}^2 \text{ s}^{-1}$, and $7.7 \cdot 10^{-16} \text{ cm}^2 \text{ s}^{-1}$ for current densities of $-4 \mu\text{A cm}^{-2}$, $-18 \mu\text{A cm}^{-2}$, and

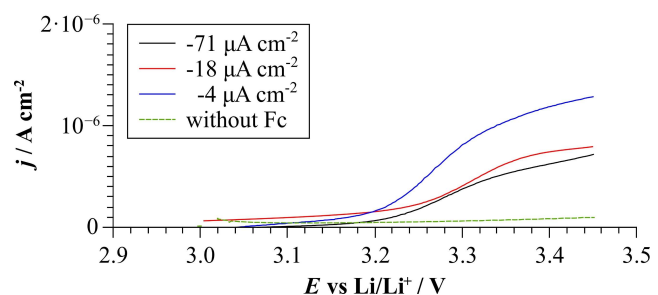


Figure 4. Voltammograms of ferrocene oxidation at a glassy carbon electrode after galvanostatic SEI formation in the LiBOB-containing electrolyte at different current densities. The green dashed line is the voltammogram obtained in a control experiment with a ferrocene-free electrolyte. (Scan rate $v = 10 \text{ mV/s}$).

$-71 \mu\text{A cm}^{-2}$, respectively. These values are also listed in Table 1.

In Figure 4, we show voltammograms obtained after forming the SEIs and exchanging the electrolyte by a ferrocene-containing electrolyte. Above the half-wave potential of ferrocene ($E_{1/2} = 3.24 \text{ V}$), the current density becomes almost constant, indicating a diffusion-limited current. Such diffusion-limited currents were also observed previously for SEIs formed by slow-scan cyclic voltammetry.^[19,20] A control experiment with a ferrocene-free electrolyte shows only very small (most likely capacitive) currents in the same potential range. These results give indication that the reduction of ferrocene is limited by the diffusive transport of ferrocene molecules across the SEI.

From the diffusion-limited current $j_{lim, anodic}$ at a potential of 3.4 V , the effective diffusion coefficient of ferrocene D_{Fc}^{eff} inside pores in the SEI was calculated using Equation (8).

$$D_{Fc}^{eff} = \frac{j_{lim, anodic} \cdot d_{SEI}}{F \cdot c_{Fc}} \quad (8)$$

where F = Faraday constant and c_{Fc} = concentration of ferrocene.

Values of the SEI thickness d_{SEI} were taken from the results of the impedance measurements assuming $\varepsilon_r = 10$. We obtain D_{Fc}^{eff} values of $2.7 \cdot 10^{-12} \text{ cm}^2 \text{ s}^{-1}$, $1.4 \cdot 10^{-12} \text{ cm}^2 \text{ s}^{-1}$ and $9.2 \cdot 10^{-13} \text{ cm}^2 \text{ s}^{-1}$ for current densities of $-4 \mu\text{A cm}^{-2}$, $18 \mu\text{A cm}^{-2}$ and $-71 \mu\text{A cm}^{-2}$, respectively. These values, also being listed in Table 1, show that the diffusion of the ferrocene molecules becomes slower with increasing current density. Here, it is important to note that the value of ε_r influences the absolute values of both $D_{Li^+}^{eff}$ and D_{Fc}^{eff} , but has no influence on the ratio of both effective diffusion coefficients.

Table 1. Overview over the SEI properties obtained from impedance, capacitance and elastance spectra.

Additive concentration	J [$\mu\text{A cm}^{-2}$]	C_{SEI} [F cm^{-2}]	d_{EIS} [nm]	$R_{SEI} (\omega_{max}^{SEI} \text{ from S-plane})$ [$\text{k}\Omega \text{ cm}^2$]	D_{Fc}^{eff} [$\text{cm}^2 \text{ s}^{-1}$]	$D_{Li^+}^{eff}$ [$\text{cm}^2 \text{ s}^{-1}$]
0 mM LiBOB	-71	$8.3 \cdot 10^{-7}$	11	32	$7.6 \cdot 10^{-12}$	$7.8 \cdot 10^{-15}$
50 mM LiBOB	-71	$6.3 \cdot 10^{-7}$	14	420	$9.2 \cdot 10^{-13}$	$7.7 \cdot 10^{-16}$
50 mM LiBOB	-18	$4.8 \cdot 10^{-7}$	19	17	$1.4 \cdot 10^{-12}$	$2.5 \cdot 10^{-14}$
50 mM LiBOB	-4	$4.0 \cdot 10^{-7}$	22	0.8	$2.7 \cdot 10^{-12}$	$6.4 \cdot 10^{-13}$

Comparing the values of $D_{Li^+}^{eff}$ and D_{Fc}^{eff} in Table 1 reveals that $D_{Li^+}^{eff}$ and D_{Fc}^{eff} exhibit similar values at the lowest formation current density of $-4 \mu A cm^{-2}$. This was also observed in previous works for SEIs formed by means of slow-scan cyclic voltammetry.^[19,20] However, with increasing formation current density, $D_{Li^+}^{eff}$ decreases much more strongly than D_{Fc}^{eff} . At the highest formation current density of $-71 \mu A cm^{-2}$, the ratio $D_{Li^+}^{eff}/D_{Fc}^{eff}$ is close to 10^{-3} , implying a much slower diffusion of the Li^+ ions across the SEI in comparison to the ferrocene molecules.

In order to verify that this discrepancy between $D_{Li^+}^{eff}$ and D_{Fc}^{eff} is not an artifact of our analysis, we calculated a hypothetical angular frequency $\omega_{max}^{SEI, hypo}$ in the $\hat{S}(\omega)$ plane under the assumption that the Li^+ ions diffuse as fast as the ferrocene molecules. This was done by taking equation (8) and inserting $D_{Li^+}^{eff} = D_{Fc}^{eff}$. In Figure 2 (d), this hypothetical angular frequency $\omega_{max}^{SEI, hypo}$ is sketched for all three formation current densities. At high current densities, $\omega_{max}^{SEI, hypo}$ is much larger than ω_{max}^{SEI} and is located in the high-frequency spike region caused by the electrolyte resistance and not in the frequency range of the SEI-related intermediate-frequency semicircle. This observation clearly excludes similar effective diffusion coefficients of Li^+ and Fc .

2.2. Fast Galvanostatic SEI Formation with and without LiBOB Additive

In order to check whether or not the high ion transport resistance of SEI formed under high current densities is a special feature of LiBOB-containing electrolytes, we carried out SEI formation in an additive-free electrolyte using a high current density of $-71 \mu A cm^{-2}$. In Figure 5, we show comparative potential vs. charge profiles for the LiBOB-free electrolyte and the LiBOB-containing electrolyte. In the case of the LiBOB-free electrolyte, the potential drops from the open circuit

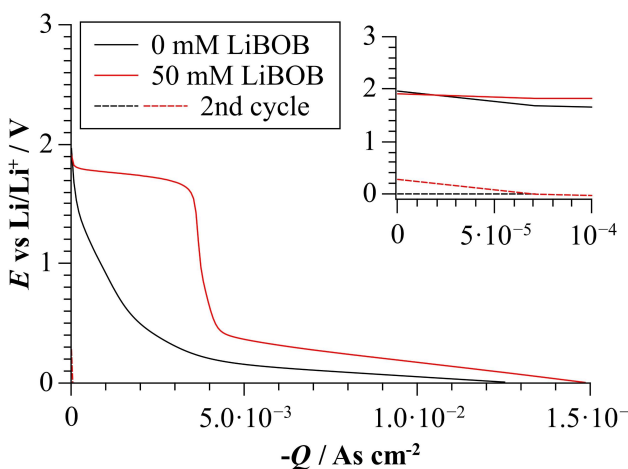


Figure 5. Electrode potential vs. charge profiles for galvanostatic SEI formation in a LiBOB-free and a LiBOB-containing electrolyte, respectively, at a current density of $-71 \mu A cm^{-2}$. The inset shows potential vs. charge profiles for the second SEI formation cycle.

potential to potentials below 0.5 V, where the major part of the SEI formation charge flow takes place. The overall charge flow is in the range of $12\text{--}15 mAs cm^{-2}$ for both electrolytes, which is lower than for SEIs formed by low-scan cyclic voltammetry (about $48 mAs cm^{-2}$ for LiBOB-free electrolyte in the first cycle^[19]). During a second galvanostatic cycle, only a very small amount of charge flow is observed, (see inset of Figure 5) confirming the passivating properties of both galvanostatically formed SEIs.

In Figure 6, we show impedance spectroscopic results obtained after SEI formation in different representations. A fit of the data in the capacitance plane (equation (3)) and estimation of the SEI thickness via equations (4) and (5) with $\epsilon_r=10$ leads to values of $d_{EIS}=14 nm$ for the LiBOB-containing electrolyte and $d_{EIS}=11 nm$ for the additive-free electrolyte. The SEI resistance was calculated from the maximum of S'' at the intermediate-frequency semicircle using equation (6). This resulted in $32 k\Omega cm^2$ for the LiBOB-free SEI as compared to $420 k\Omega cm^2$ for the LiBOB containing SEI. Finally, we used equation (7) for calculating the effective diffusion coefficients of the Li^+ ions and obtained values of $D_{Li^+}^{eff}=7.8 \cdot 10^{-15} cm^2 s^{-1}$ for the additive-free electrolyte as compared to $D_{Li^+}^{eff}=7.7 \cdot 10^{-16} cm^2 s^{-1}$ for the LiBOB-containing electrolyte, see Table 1.

After exchanging the electrolyte for a ferrocene-containing electrolyte, the voltammogram obtained for the additive-free electrolyte is shown as a black line in Figure 7. For comparison, we also show the voltammogram for the LiBOB-containing electrolyte. Both voltammograms give indication for a diffusion-limited current, which was used for calculating the effective diffusion coefficient of the ferrocene molecules. From the diffusion-limited current at 3.4 V, values of $D_{Fc}^{eff}=7.6 \cdot 10^{-12} cm^2 s^{-1}$ for the LiBOB-free electrolyte and $D_{Fc}^{eff}=9.2 \cdot 10^{-13} cm^2 s^{-1}$ for the LiBOB-containing electrolyte were obtained.

In order to obtain complementary information about the SEI thickness, we carried out AFM scratching experiments. In Figure 8, the topographic AFM images of the galvanostatically formed SEIs are shown. By applying a high force of $1.5 \mu N$ to the AFM tip, the SEI could be completely removed inside the scratching windows in the center of the topographic images. SEI thickness of $d_{AFM}=20 nm$ and $d_{AFM}=80 nm$ were obtained for the additive-free electrolyte and for the LiBOB-containing electrolyte, respectively, see Table 2. When comparing the SEI thickness obtained from the impedance data and from the AFM scratching experiments, it is obvious that d_{EIS} and d_{AFM} are quite similar in the case of the additive-free electrolyte. Assuming a relative permittivity of about $\epsilon_r=20$ would lead to identical values for d_{EIS} and d_{AFM} , as was also observed in previous studies

Table 2. Comparison of SEI thickness values obtained from AFM scratching experiments (d_{AFM}) and estimated from impedance spectra (d_{EIS}).

Electrolyte	$1 M LiPF_6$ in 30/30/40 EC/EMC/DMC	$1 M LiPF_6$ in 30/30/40 EC/EMC/DMC + 50 mM LiBOB
d_{AFM} [nm]	20	80
d_{EIS} [nm]	9	18

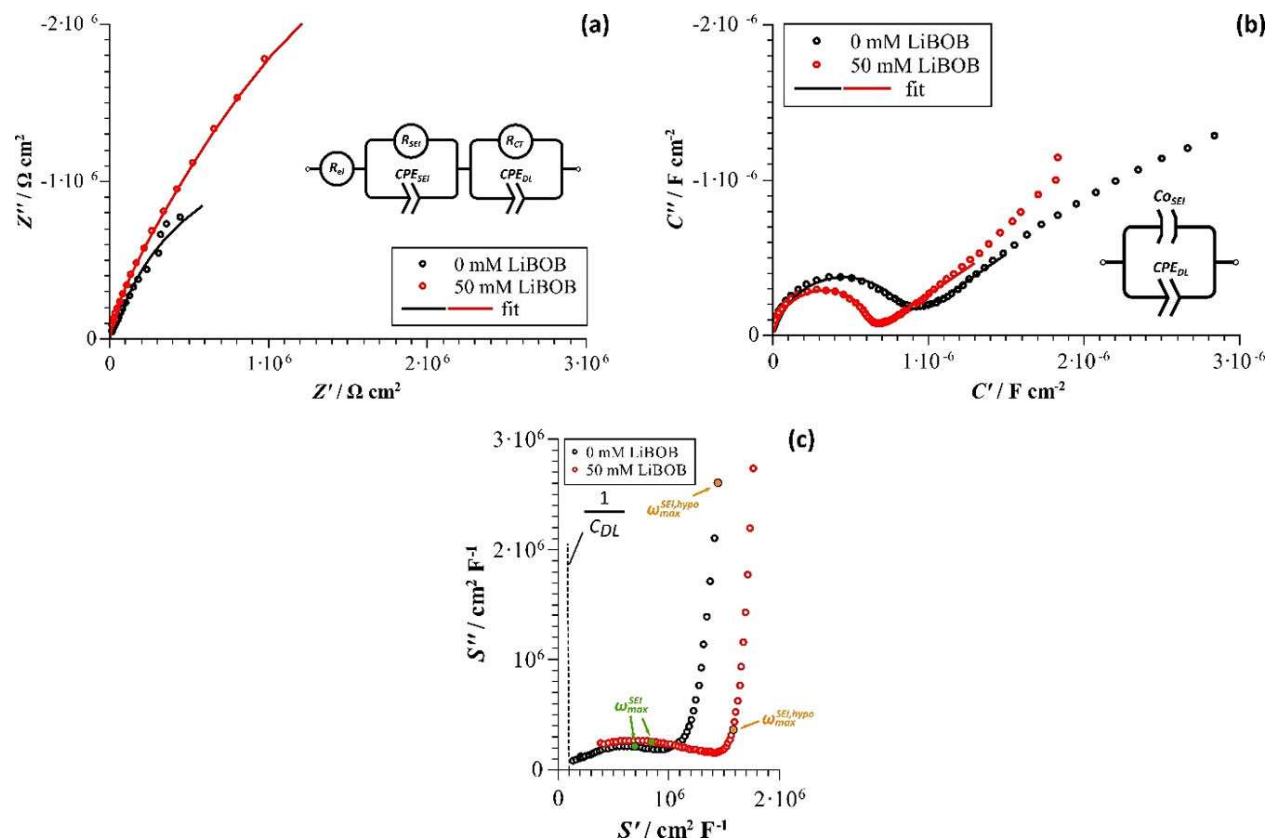


Figure 6. a) Impedance spectra, b) capacitance spectra, and c) elastance spectra obtained after SEI formation in a LiBOB-free and a LiBOB-containing electrolyte, respectively, at a current density of $-71 \mu\text{A cm}^{-2}$.

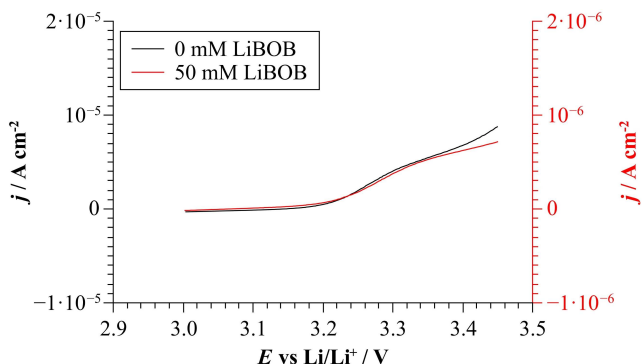


Figure 7. Voltammograms of ferrocene oxidation at a glassy carbon electrode after galvanostatic SEI formation in a LiBOB-free and a LiBOB-containing electrolyte, respectively, at a current density of $-71 \mu\text{A cm}^{-2}$. (Scan rate $v = 10 \text{ mV/s}$).

on SEIs formed by means of slow-scan cyclic voltammetry.^[19] However, in the case of the LiBOB-containing electrolyte, d_{AFM} is much larger than d_{EIS} , suggesting that only a part of the SEI layer contributes to the passivating properties.

2.3. Activation Energies of Effective Diffusion Coefficients

In order to determine activation energies of effective diffusion coefficients, temperature-dependent transport measurements

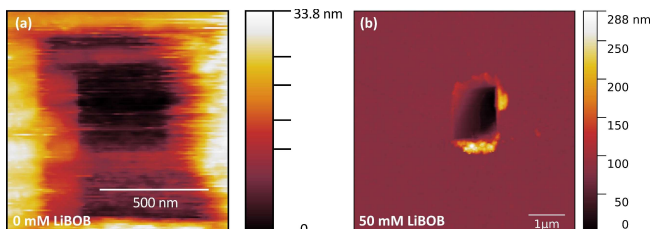


Figure 8. AFM topographic images of the galvanostatically formed SEIs ($j = -71 \mu\text{A cm}^{-2}$), with a scratching crater in the center. a) SEI formed in the LiBOB-free carbonate electrolyte. b) SEI formed in the carbonate electrolyte with 50 mM LiBOB.

were carried out on two exemplary SEIs: (i) An SEI formed with the highest current density of $-71 \mu\text{A cm}^{-2}$ in the LiBOB-containing electrolyte. At this SEI, the ratio of effective diffusion coefficients $D_{\text{Li}^+}^{\text{eff}}/D_{\text{Fc}}^{\text{eff}}$ is close to 10^{-3} . (ii) An SEI formed via slow-scan cyclic voltammetry as reported in [19]. At this SEI, the ratio of effective diffusion coefficients $D_{\text{Li}^+}^{\text{eff}}/D_{\text{Fc}}^{\text{eff}}$ is close to unity.

Impedance measurements at 3 V vs. Li/Li^+ and redox probe cyclic voltammetry between 3 V and 3.45 V vs. Li/Li^+ were carried out at temperatures between 5 °C and 25 °C. In this temperature range, no irreversible changes in the transport properties of the SEIs upon heating and cooling were observed. The measurements were started at 25 °C, then the cells were cooled down to 5 °C and heated up to 25 °C with temperature intervals of 5 °C. The activation energies E_A of the effective

diffusion coefficients were then obtained from an Arrhenius plot of the temperature-dependent $D^{\text{eff}}(T)$ data [Eq. (9)].

$$D^{\text{eff}}(T) = D_0 \cdot \exp\left(-\frac{E_A}{RT}\right) \quad (9)$$

where D_0 denotes the preexponential factor of the effective diffusion coefficient.

Impedance spectra and redox probe cyclic voltammograms for the SEI formed via slow-scan cyclic voltammetry are shown in Figure 9 (a) and (b). Here, the SEI resistance could be obtained with high accuracy from a fit of the impedance data in $\hat{Z}(\omega)$ plane. The results for the galvanostatically formed SEI are shown in Figure 9 (c) and (d). In this case, the ionic diffusion coefficient was calculated from $\omega_{\max}^{\text{SEI}}$ in the $\hat{S}(\omega)$ plane as described by equation (7) previously. As already shown in Figs. 2 and 3, $\omega_{\max}^{\text{SEI}}$ was chosen as the angular frequency at half distance between $S' = \frac{1}{AC} \approx \frac{1}{C_{\text{SEI}}}$ at high frequencies and $S' = \frac{1}{C_{\text{DL}}}$ at low frequencies. Due to the non-ideal shape of the SEI semicircle (suppressed semicircle) in the $\hat{S}(\omega)$ plane, we think that a factor of 3 is a reasonable conservative estimate of

the uncertainty of $\omega_{\max}^{\text{SEI}}$, see also our simulation results in the Supporting Information.

Figure 9 (b) and (d) clearly reveal the increase of the ferrocene diffusion-limited current with increasing temperature. The Arrhenius plots of the effective diffusion coefficients are shown in Figure 10. For comparison, the diffusion coefficients of Li^+ and ferrocene in the neat bulk electrolyte are shown as well, which were obtained from standard ion conductivity measurements and standard cyclic voltammetry combined with Randles-Sevcik analysis. The activation energies obtained from the Arrhenius fits are given in Table 3.

In the neat bulk electrolyte, the activation energy for both Li^+ diffusion and ferrocene diffusion are 0.12 eV and 0.11 eV, respectively. These values are in good agreement with literature reports on similar electrolytes.^[30] In the case of the SEI formed by slow-scan cyclic voltammetry, the activation energy for Li^+ diffusion and ferrocene diffusion is also similar, namely 0.29 eV and 0.26 eV. These values are, however, much higher than that in the neat bulk electrolyte. Based on the very similar effective diffusion coefficients $D_{\text{Li}^+}^{\text{eff}}$ and $D_{\text{Fc}}^{\text{eff}}$ in this SEI, we have argued that both ions and molecules are transported across the liquid electrolyte inside the pores of the SEI.^[19,20] Under this

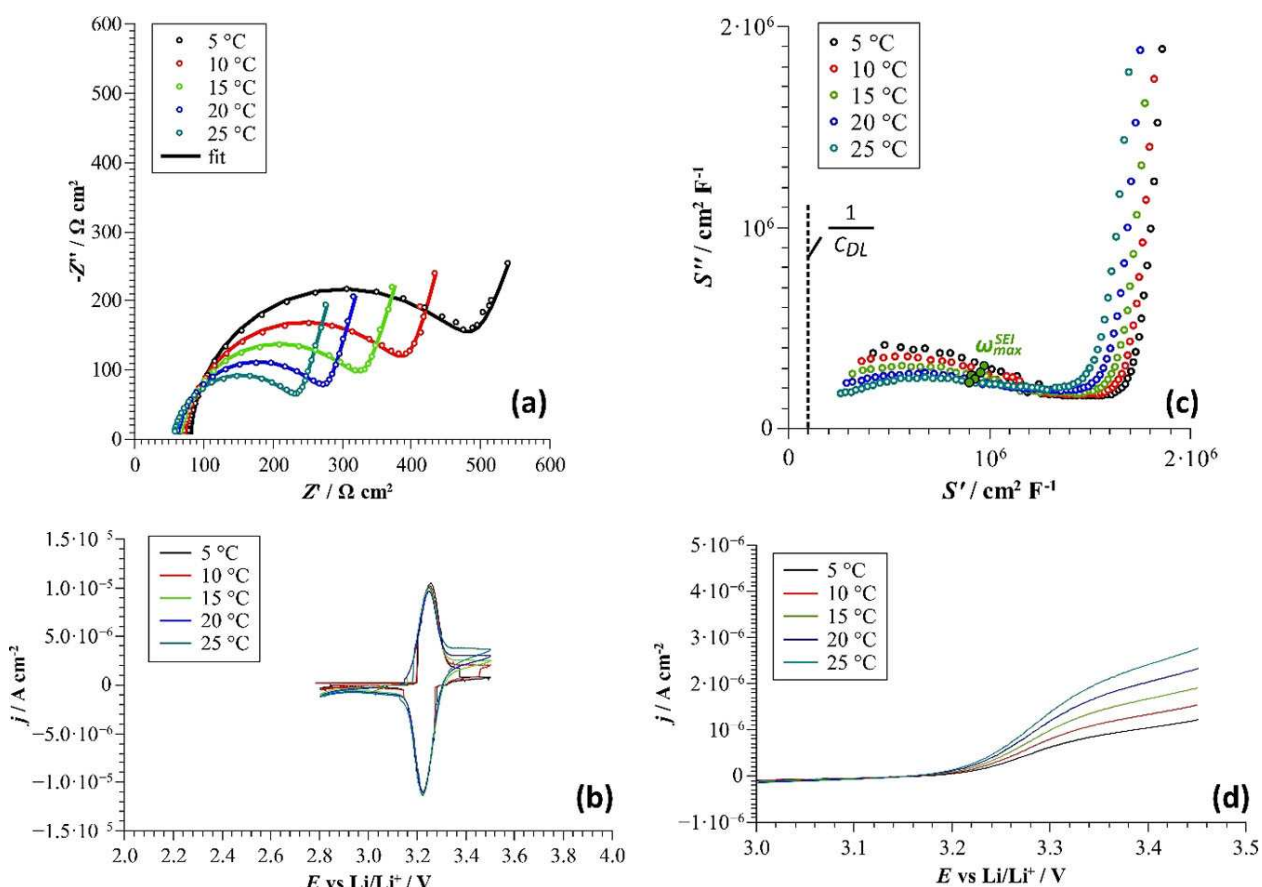


Figure 9. a) Temperature-dependent impedance spectra of a glassy carbon electrode after SEI formation in a LiBOB-free electrolyte by slow-rate cyclic voltammetry according to Ref. [19]. b) Temperature-dependent cyclic voltammograms for ferrocene oxidation / ferrocenium reduction at a glassy carbon electrode after SEI formation in a LiBOB-free electrolyte by slow-rate cyclic voltammetry according to Ref. [19]. c) Temperature-dependent elastance spectra of a glassy carbon electrode after galvanostatic SEI formation in a 50 mM LiBOB containing electrolyte at a current density of $-71 \mu\text{A cm}^{-2}$. d) Temperature-dependent voltammograms for ferrocene oxidation at a glassy carbon electrode after galvanostatic SEI formation in a 50 mM LiBOB containing electrolyte at a current density of $-71 \mu\text{A cm}^{-2}$.

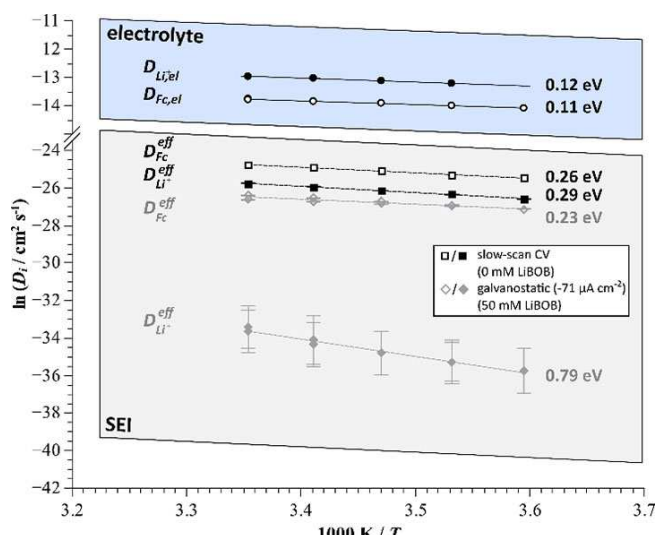


Figure 10. Arrhenius plot of the effective diffusion coefficients of Li^+ ions, $D_{\text{Li}^+}^{\text{eff}}$, and of the ferrocene molecules, $D_{\text{Fc}}^{\text{eff}}$, in SEIs formed under different conditions. For comparison, the diffusion coefficients of Li^+ ions and ferrocene molecules in the neat bulk electrolyte, $D_{\text{Li}^+, \text{el}}$ and $D_{\text{Fc}, \text{el}}$ are shown in the upper part of the figure. For each measurement data from the heating and the cooling process are plotted.

assumption, a higher activation energy for the pore transport suggests that the transport is influenced by the confinement of the liquid electrolyte in the pores of the SEI. The similar activation energies of $D_{\text{Li}^+}^{\text{eff}}$ and $D_{\text{Fc}}^{\text{eff}}$ indicate that the entire dynamics of the liquid electrolyte containing ions and ferrocene molecules is slowed down by the interaction with the pore walls. However, in the case of the SEI formed galvanostatically with high current density, the activation energies of $D_{\text{Li}^+}^{\text{eff}}$ and $D_{\text{Fc}}^{\text{eff}}$ differ strongly. The activation energy for ferrocene diffusion is 0.23 eV, i.e. similar to the activation energy obtained for the SEI formed via slow-scan cyclic voltammetry. However, the activation energy for the Li^+ ion transport is much higher, namely 0.79 eV. This implies that the galvanostatically formed SEI shows selectivity for the transport of different species.

It is well known that transport through micro- and mesopores often leads to a selectivity for different ions and/or molecules based on different mechanisms, e.g. size exclusion, wettability of the pore walls or specific interactions of ions/molecules with the pore walls (nanofiltration, ion sieving).^[31–33]

Recently, Harris and Tang suggested a chemical selectivity of the SEI based on different partition coefficients of polar and non-polar molecules between the bulk electrolyte and the SEI.^[26] In order to further test this hypothesis, the future use of chemical modified redox molecules with different charge, size and functionalities is recommendable. Furthermore, transport selectivities seem to play an important role for overcharge-protection in lithium-ion batteries. Several groups reported^[34–36] that overcharge-protection additives, which are redox molecules, work successfully in conventional lithium-ion batteries. In these batteries, overcharging leads to oxidation of the redox molecules at the positive electrode, diffusion of the redox molecules to the negative electrode and reduction of the redox molecules at the negative electrode, despite the existence of the SEI. It is unclear why the graphite SEI allows for a fast reduction of the redox molecules, but inhibits reduction of the carbonate molecules. Li *et al.* showed that ion transport across SEIs on graphite is not limited to Li^+ ion transport, but also anions can be transported.^[38] They formed an SEI on graphite particles by reductive decomposition of the electrolyte and then used these graphite particles as positive electrode in a dual-ion cell, in which PF_6^- anions are reversible intercalated in the positive electrode. This implies that PF_6^- anion transport across the SEI is possible. Most likely, the anions are transported across electrolyte-filled pores of the SEI, since solid-state PF_6^- anion transport is unknown.

At present, the transport mechanism of the Li^+ ions across the galvanostatically formed SEI is not clear. It is conceivable that the Li^+ ions are either transported very slowly across the pores due to specific ion/pore wall interactions or pore transport is so strongly hindered that the Li^+ ions move across the solid phase of the SEI, e.g. along grain boundaries.^[37] Independent of which transport mechanism predominates, our results imply that ion transport across the solid phase of the SEI must be very slow. Thus, it seems that fast Li^+ ion transport across the SEI can only be achieved when fast pore transport is possible, as in the case of the SEI formed by slow-scan cyclic voltammetry.

Table 3. Activation energies E_A and preexponential factors D_0 of the effective diffusion coefficients of Li^+ ions, $D_{\text{Li}^+}^{\text{eff}}$, and of ferrocene molecules, $D_{\text{Fc}}^{\text{eff}}$, in SEIs formed under different conditions. For comparison, activation energies and pre-exponential factors are also given for the diffusion coefficients of Li^+ ions and ferrocene molecules in the neat bulk electrolyte, $D_{\text{Li}^+, \text{el}}$ and $D_{\text{Fc}, \text{el}}$.

C_{LiBOB} [mol L ⁻¹]	Formation conditions	E_A [eV]	D_0 [cm ² s ⁻¹]
$D_{\text{Li}^+, \text{el}}$	50	–	$2.8 \cdot 10^{-4} \pm 4.7\%$
$D_{\text{Fc}, \text{el}}$	50	–	$7.7 \cdot 10^{-5} \pm 35.6\%$
$D_{\text{Li}^+}^{\text{eff}}$	0	CV (0.5 mVs ⁻¹)	$0.29 \pm 2.4\%$
$D_{\text{Fc}}^{\text{eff}}$	0	CV (0.5 mVs ⁻¹)	$0.26 \pm 1.6\%$
$D_{\text{Li}^+}^{\text{eff}}$	50	galv ($-71 \mu\text{A cm}^{-2}$)	$0.79 \pm 53\%$
$D_{\text{Fc}}^{\text{eff}}$	50	galv ($-71 \mu\text{A cm}^{-2}$)	$0.23 \pm 2.2\%$

2.4. Maximum Area-Specific SEI Resistance Tolerable in Commercial Lithium-Ion Batteries

In the case of the galvanostatically formed SEIs, the area-specific resistance of the SEI increases from $0.8 \text{ k}\Omega \text{ cm}^2$ for the lowest current density to about $420 \text{ k}\Omega \text{ cm}^2$ for the highest current density. In the following, we estimate what maximum area-specific SEI resistance is still tolerable in a commercial lithium-ion battery. As an example, we take the 18650 lithium-ion battery cell from Panasonic, purchased by ENERdan GmbH, with a voltage of 3.7 V and a capacity of 2900 mAh. Since the theoretical capacity of graphite is 372 mAh g^{-1} ^[39], the mass of graphite needed to store 2900 mAh is about 8 g. The BET area of typical graphite particles used in lithium-ion batteries is about $3 \text{ m}^2 \text{ g}^{-1}$,^[40] so that the overall surface area of the graphite in the cell should be about 24 m^2 . The AC resistance of the total cell is $< 160 \text{ m}\Omega$ at a frequency of 1 kHz.^[41] Due to the existence of various impedances in such a cell, we now make the assumption that not more than 1/3 of the $160 \text{ m}\Omega$ resistance should be caused by the SEI. Taking into account the overall surface area of the graphite particles, this corresponds to a maximum area-specific SEI resistance of about $12 \text{ k}\Omega \text{ cm}^2$. Only the resistance of the SEI formed with the lowest current density of $-4 \mu\text{A cm}^{-2}$ is below this maximum value, while the resistance of the SEI formed at the highest current density of $-71 \mu\text{A cm}^{-2}$ exceeds the maximum value by more than one order of magnitude. This result indicates that a too fast galvanostatic formation of the SEI in commercial batteries would lead to Li^+ ion transport resistances clearly exceeding the maximum tolerable value.

3. Conclusions

We have shown that the current density during galvanostatic SEI formation exerts a strong influence on the transport properties of the SEI. At the lowest formation current of $-4 \mu\text{A cm}^{-2}$, the effective diffusion coefficient of the Li^+ ions, $D_{\text{Li}^+}^{\text{eff}}$, and the effective diffusion coefficient of ferrocene redox molecules, $D_{\text{Fc}}^{\text{eff}}$, exhibit very similar values, as also observed in previous experiments on SEIs formed via slow-scan cyclic voltammetry.^[19,20] This indicates that both Li^+ ions and ferrocene molecules are transported across the electrolyte-filled pores of the SEI. With increasing formation current density, the transport of both Li^+ ions and the ferrocene molecules is slowed down, but the effect is much stronger for the Li^+ ions. At the highest formation current density of $-71 \mu\text{A cm}^{-2}$, $D_{\text{Li}^+}^{\text{eff}}$ is almost three orders of magnitude lower than $D_{\text{Fc}}^{\text{eff}}$. This goes along with a much higher activation energy for the ionic transport than for the ferrocene transport. These results point to selective transport of the SEI formed at high current densities. It is conceivable that either the Li^+ ions interact very strongly with the pore walls resulting in very slow pore transport or that pore transport is so strongly hindered that the Li^+ ions move across the solid phase of the SEI, possibly along grain boundaries. In any case, it seems that fast Li^+ ion

transport across SEIs can only be achieved, if fast pore transport of the Li^+ ions is possible.

Finally, we have estimated the maximum tolerable area-specific resistance of the SEI in a commercial lithium-ion battery cell, which is in the range of $10 \text{ k}\Omega \text{ cm}^2$. At low formation current densities, the area-specific resistance of our model-type SEI is below this maximum tolerable value, but at the highest formation current density of $-71 \mu\text{A cm}^{-2}$, the area-specific resistance of the SEI clearly exceed the tolerable range.

Acknowledgements

We are grateful to the State of Hesse for providing basic financing for this project. Furthermore, we thank Albemarle Corporation for providing lithium foil.

Conflict of Interest

The authors declare no conflict of interest.

Keywords: lithium-ion batteries · solid electrolyte interphase · ion transport · passivation · redox-probe-voltammetry

- [1] E. Peled, *J. Electrochem. Soc.* **1979**, *126*, 2047–2051.
- [2] D. Aurbach, A. Zaban, I. Weissman, B. Markovsky, M. Levi, E. Levi, A. Schechter, E. Granot, *J. Power* **1997**, *68*, 91–98.
- [3] J. O. Besenhard, M. Winter, J. Yang, W. Biberacher, *J. Power Sources* **1995**, *54*, 228–231.
- [4] S. Huang, S. Wang, G. Hu, L. Z. Cheong, C. Shen, *Appl. Surf. Sci.* **2018**, *441*, 265–271.
- [5] X.-B. Cheng, R. Zhang, C.-Z. Zhao, F. Wei, J.-G. Zhang, Q. Zhang, *Adv. Sci.* **2016**, *3*, 1500213.
- [6] J. Zhang, X. Yang, R. Wang, W. Dong, W. Lu, X. Wu, X. Wang, H. Li, L. Chen, *J. Phys. Chem. C* **2014**, *118*, 20756–20762.
- [7] N. P. W. Pieczenka, L. Yang, M. P. Balogh, B. R. Powell, K. R. Chemelewski, A. Manthiram, S. A. Krachkovskiy, G. R. Goward, M. Liu, J. Kim, *J. Phys. Chem. C* **2013**, *117*, 22603–22612.
- [8] T. R. Jow, S. A. Delp, J. L. Allen, J.-P. Jones, M. C. Smart, *J. Electrochem. Soc.* **2018**, *165*, A361–A367.
- [9] M. Winter, *Z. Phys. Chemie* **2009**, *223*, 1395–1406.
- [10] D. L. Wood, J. Li, C. Daniel, *J. Power Sources* **2015**, *275*, 234–242.
- [11] B. K. Antonopoulos, C. Stock, F. Maglia, H. E. Hoster, *Electrochim. Acta* **2018**, *269*, 331–339.
- [12] S. Bhattacharya, A. R. Riahi, A. T. Alpas, *MRS Online Proceedings Library Archive* **2012**, 1388.
- [13] S. Bhattacharya, A. T. Alpas, *Carbon* **2012**, *50*, 5359–5371.
- [14] S. J. An, J. Li, Z. Du, C. Daniel, D. L. Wood, *J. Power Sources* **2017**, *342*, 846–852.
- [15] E. Budevski, G. Staikov, W. J. Lorenz, *Electrochim. Acta* **2000**, *45*, 2559–2574.
- [16] S. Lau, L. A. Archer, *Nano Lett.* **2015**, *15*, 5995–6002.
- [17] B. K. Antonopoulos, F. Maglia, F. Schmidt-Stein, S. J. P. Schmidt, H. E. Hoster, *Batteries&Supercaps* **2018**, *1*, 110–121.
- [18] W. Märkle, C.-Y. Lu, P. Novak, *J. Electrochem. Soc.* **2011**, *158*, A1478–A1482.
- [19] T. Kranz, S. Kranz, V. Miß, J. Schepp, B. Roling, *J. Electrochem. Soc.* **2017**, *164*, A3777–A3784.
- [20] S. Kranz, T. Kranz, A. G. Jaegermann, B. Roling, *J. Power Sources* **2019**, *418*, 138–146.
- [21] M. Tang, J. Newman, *J. Electrochem. Soc.* **2011**, *158*, A530–A536.
- [22] M. Tang, S. Lu, J. Newman, *J. Electrochem. Soc.* **2012**, *159*, A1775–A1785.
- [23] M. Tang, J. Newman, *J. Electrochem. Soc.* **2012**, *159*, A281–A289.

- [24] R. R. Jaini, B. P. Setzler, A. G. Star, T. F. Fuller, *J. Electrochem. Soc.* **2016**, *163*, A2185–A2196.
- [25] M. T. Dinh-Nguyen, C. Delacourt, *J. Electrochem. Soc.* **2016**, *163*, A706–A713.
- [26] O. C. Harris, M. H. Tang, *J. Phys. Chem. C* **2018**, *122*, 20632–20641.
- [27] Z. Chen, W. Q. Lu, J. Liu, K. Amine, *Electrochim. Acta* **2006**, *51*, 3322–3326.
- [28] J. R. Macdonald, W. B. Johnson, *Fundamentals of Impedance Spectroscopy in Impedance spectroscopy. Theory, experiment and applications*, 2nd edition, Wiley-Interscience, Hoboken, New Jersey, **2005**.
- [29] S. A. Krachkovskiy, J. D. Bazak, S. Fraser, I. C. Halalay, G. R. Goward, *J. Electrochem. Soc.* **2017**, *164*, A912–A916.
- [30] M. Z. Kufian, S. R. Majid, *Ionics* **2010**, *16*, 409–416.
- [31] Z. Zhu, D. Wang, Y. Tian, L. Jiang, *J. Am. Chem. Soc.* **2019**, *141*, 8658–8669.
- [32] I. Vlassiouk, S. Smirnov, Z. Siwy, *Nano Lett.* **2008**, *8*, 1978–1985.
- [33] Z. Zhang, X. Sui, P. Li, G. Xie, X.-Y. Kong, K. Xiao, L. Gao, L. Wen, L. Jiang, *J. Am. Chem. Soc.* **2017**, *139*, 8905–8914.
- [34] J. Chen, C. Buhrmester, J. R. Dahn, *Electrochim. Solid-State Lett.* **2005**, *8*, A59–A62.
- [35] J. Zhang, I. A. Shkrob, R. S. Assary, S. Zhang, B. Hu, C. Liao, Z. Zhang, L. Zhang, *J. Power Sources* **2018**, *378*, 264–267.
- [36] O. Leonet, L. C. Colmenares, A. Kvasha, M. Oyarbide, A. R. Mainar, T. Glossmann, J. A. Blázquez, Z. Zhang, *ACS Appl. Mater. Interfaces* **2018**, *10*, 9216–9219.
- [37] A. Ramasubramanian, V. Yurkiv, T. Foroozan, M. Ragone, R. Shahbazian-yassar, F. Mashayek, *J. Phys. Chem. C* **2019**, *123*, 10237–10245.
- [38] W.-H. Li, Q.-L. Ning, X.-T. Xi, B.-H. Hou, J.-Z. Guo, Y. Yang, B. Chen, X.-L. Wu, *Adv. Mater.* **2019**, *31*, 1804766–1804766.
- [39] P. Guo, H. Song, X. Chen, *Electrochim. Commun.* **2009**, *11*, 1320–1324.
- [40] Pyrotek, 'Pyrotek, Battery Materials - Graphite Anode Materials for Lithium-ion Batteries', can be found under: https://www.pyrotek.com/our-solutions/battery-materials/index?Locale=en_GB, **10.09.2019**.
- [41] ENERdan GmbH, '3,7 V Lithium-Ionen Akkumulator 18650 mit PCB (5 A/7 A), 2900 mAh', data sheet, can be found under: http://www.produktinfo.conrad.com/datenblaetter/250000-274999/251602-da-01-de-ENERDAN_LIION_AKU_18650_2900_MAH.pdf, **10.09.2019**.
- [42] B. Hirschorn, M. E. Orazem, B. Tribollet, V. Vivier, I. Frateur, M. Musiani, *Electrochim. Acta* **2010**, *55*, 6218–6227.

Manuscript received: August 12, 2019

Revised manuscript received: September 13, 2019

Version of record online: October 4, 2019